Inorganic Chemistry

ARTICLE

pubs.acs.org/IC

Ordering Double Perovskite Hydroxides by Kinetically Controlled Aqueous Hydrolysis

James R. Neilson,[†,‡,§] Joshua A. Kurzman,[‡,∥] Ram Seshadri,[‡,∥,⊥] and Daniel E. Morse*[,†,‡,§]

[†]Biomolecular Science & Engineering, [‡]Materials Research Laboratory, [§]Institute for Collaborative Biotechnologies, [∥]Department of Chemistry and Biochemistry, and [⊥]Materials Department, University of California Santa Barbara, Santa Barbara, California 93106, United States

ABSTRACT: The precipitation of crystals with stoichiometric and ordered arrangements of distinct metal cations often requires carefully designed molecular precursors and/or sufficient activation energy in addition to the necessary mass transport. Here, we study the formation of ordered double perovskite hydroxides, $MnSn(OH)_6$ and $CoSn(OH)_6$, of the generic chemical formula, $BB'(OH)_6$ (no *A* site), using kinetic control of aqueous hydrolysis from simple metal salt solutions. We find that the precipitation yields ordered compounds only when the *B* ion is Mn(II) or Co(II), and not when it is any other divalent transition metal ion, or Zn(II). The key step in forming the compounds is the prevention of rapid and uncontrolled hydrolysis of Sn(IV), and this is achieved by a fluoride counteranion. The two compounds, $MnSn(OH)_6$ and $CoSn(OH)_6$, are studied by high-resolution synchrotron X-ray diffraction and from the temperature dependence of magnetic behavior. From maximum entropy image restoration of the electron density and from Rietveld analysis, the degree of octahedral distortion and tilting and the small extent of anti-site disorder are determined. From the nonoverlapping electron density, we infer strongly ionic character of bonding. As the first magnetic study of such materials, we report simple paramagnetic behavior with no long-range magnetic order down to 2 K for the Mn(II) compound, while the cobalt compound presents uncompensated antiferromagnetic interactions, attributed to the single-ion anisotropy of octahedral Co(II).

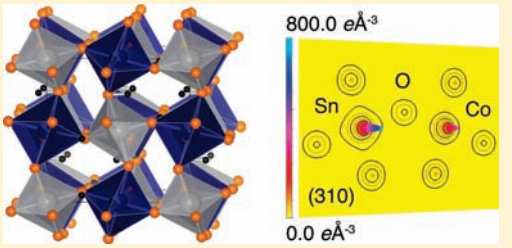

INTRODUCTION

Kinetic control of aqueous hydrolysis offers a method to systematically prepare metastable compounds or materials with unusual morphologies, as we have reported with the structural variation of α-type cobalt hydroxide chlorides[1] and the formation of cubic nanoparticles of CeO_2.[2] However, the preparation of stoichiometrically ordered bimetallic materials using kinetic control typically requires complex bimetallic molecular precursors, as we have seen with the preparation of crystalline $BaTiO_3$ nanoparticles.[3] It was hypothesized that the bimetallic molecular precursor prevents uncontrolled hydrolysis of the two dissimilar cations (Ti^{4+}, Ba^{2+}) and allows them to stay in proximity to aid product formation.

In the study described here, we hypothesize that weak and cooperative interactions during kinetically controlled aqueous hydrolysis can enable the formation of ordered double perovskite hydroxides, $BB'(OH)_6$, from the controlled partial hydrolysis of two distinct monometallic molecular precursors. We attribute the cation ordering to an active role of counteranions and the hydrolysis characteristics of individual metal ions.

The crystalline double perovskite hydroxides, produced from the reaction of hydrated metal salts with a hydrolytic catalyst, exhibit long-range periodicity of alternating cations, with the connectivity of a ReO_3 lattice, shown in Figure 1. These compounds are known as the minerals Schoenfliesite, $MgSn(OH)_6$, Wickmanite, $MnSn(OH)_6$, and Burtite, $CaSn(OH)_6$.[4−6] To overcome reaction activation energy barriers, typical preparation routes of these compounds rely on elevated temperatures[7−9] or solid-state metathesis driven by the high lattice energy of a byproduct (such as NaCl).[10,11]

In this article, we identify the critical requirements for controlling the hydrolysis of dissimilar metal cations to yield such ordered perovskite hydroxides and why only certain transition metal ions can be incorporated into the lattice via low-temperature kinetic control of hydrolysis. The atomic positions of the successfully isolated compounds, $MnSn(OH)_6$ and $CoSn(OH)_6$, are located using synchrotron X-ray powder diffraction. The structures contain distorted metal−oxygen octahedra with partial anti-site disorder. The fidelity of the data allows location of the hydrogen positions. Magnetization measurements performed for the first time on these compounds, identify both crystals as paramagnets. However, $CoSn(OH)_6$ exhibits slight deviations from ideality, which we attribute to single-ion anisotropy. This study systematically analyzes the hydrolysis behavior of individual solutes and the structures of the resulting products to identify the essential requirements for forming ordered lattices in kinetically controlled precipitation reactions.

EXPERIMENTAL SECTION

Preparation. To provide kinetic control of hydrolysis, all attempted preparations were performed under identical conditions. All water used was deionized to a resistivity less than 18 MΩ cm^{-1} using a Milli-Q water treatment system. All reagents were purchased from Sigma-Aldrich unless

Received: December 15, 2010
Published: March 07, 2011

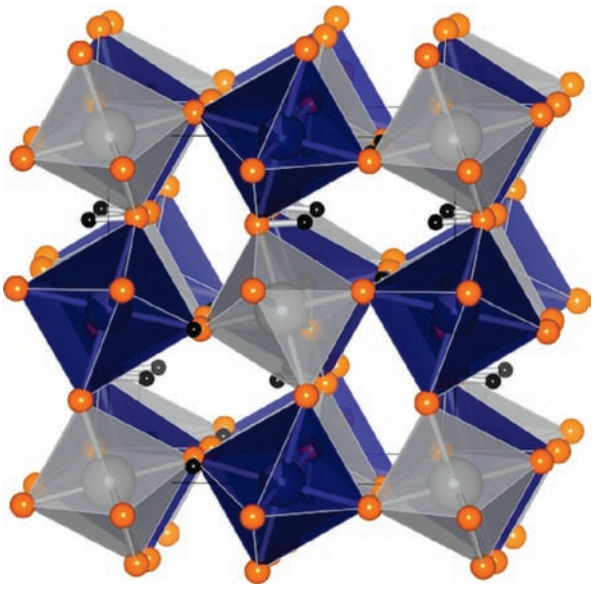

Figure 1. Structure of $MnSn(OH)_6$ as determined from synchrotron X-ray powder diffraction, showing octahedral tilting, the location of all atoms (including hydrogen), and a small degree of anti-site disorder. Gray octahedra indicate tin, blue is manganese, orange is oxygen, and black is hydrogen.

otherwise noted. Aqueous solutions containing both 0.1 M $(NH_4)_2SnF_6$ and 0.1 M metal chloride ($MnCl_2 \cdot 6H_2O$, $CoCl_2 \cdot 6H_2O$, $NiCl_2 \cdot 6H_2O$, $CuCl_2 \cdot 6H_2O$, $ZnCl_2 \cdot 6H_2O$) were prepared and stored in plastic bottles. Iron was avoided because of its disposition toward oxidation in aqueous solutions. The hydrolytic catalyst, NH_3, is prepared by dilution of a 14 M aqueous solution of NH_3 (NH_4OH, EMD Chemicals Inc.) to a concentration of 0.5 M $NH_{3(aq)}$ (~1.2 vol%).

For the kinetically controlled precipitation reaction, 5 mL aliquots of each metal precursor solution containing both metals were distributed into small plastic Petri dishes (35 mm diameter; 10 mm depth). Plastic dishes were utilized to prevent leaching of silicon from glassware by evolved HF. Great caution must be taken when working with reacted solutions, as they likely contain a significant concentration of the toxic weak acid, HF. Four of these filled dishes were then arranged in a desiccator (3 L volume). Two more Petri dishes were enclosed in the desiccator, each filled with 5 mL of the 0.5 M $NH_{3(aq)}$ solution. The desiccator was immediately sealed and left undisturbed at room temperature for 6 h.

Only the solutions containing $MnCl_2 \cdot 6H_2O$ and $CoCl_2 \cdot 6H_2O$ yielded a continuous thin film at the meniscus of the Petri dishes, indicating that those materials were formed from kinetic control of the hydrolysis. The films were isolated using a Langmuir−Blodgett technique, rinsed three times with deionized water, and dried over filter paper for 12 h at 55 °C. The powders were finely ground in an agate mortar and pestle for further characterization.

Composition and Color. The compositions of both materials were obtained from energy dispersive spectroscopy (EDS), with data acquired on a Tescan Vega 5130 scanning electron microscope (SEM) using an iXRF energy dispersive spectrometer (EDS) operating at 20 kV with a 4.0 s time constant, counting for 100 s live time. The average of 5 locations on uncoated samples at a 5000× operating magnification and a constant working distance was used to compute the tabulated compositions (Table 1). Trace quantities (1−3%) of fluorine were observed in some regions; however, overlap of the fluorine *K*-edge with the Sn *L*-edge X-ray emission lines does not allow precise quantification of the fluorine content. Photographs of the powders were captured using a Nikon Coolpix P5100 Digital camera in an uncompressed format.

Synchrotron Powder X-ray Diffraction. Ground powders (~10−20 mg) were packed into small Kapton capillaries and sealed at both ends with epoxy. Powder X-ray diffraction patterns of the loaded

Table 1. Summary of Compositions from Energy Dispersive Spectroscopy[a]

compound	Mn or Co	Sn	O
ideal	12.5	12.5	75
$MnSn(OH)_6$	11.0 ± 1.7	10.8 ± 1.1	76.5 ± 3.2
$CoSn(OH)_6$	10.4 ± 1.0	12.8 ± 0.9	77.3 ± 1.6

[a] In relative at%± std. dev.

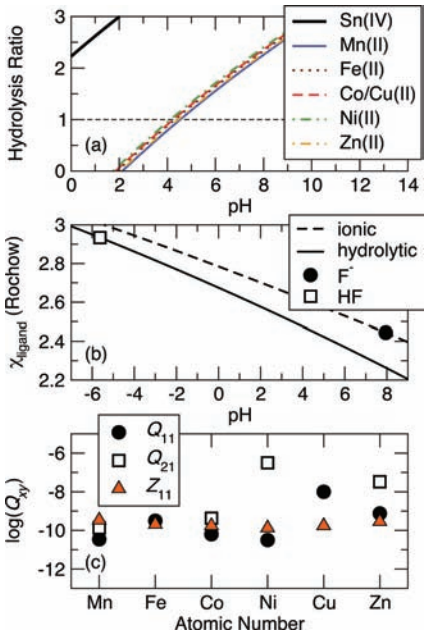

Figure 2. (a) Hydrolysis behavior of the hydrated metal ions, as predicted by the partial charge model of Livage,[21] indicating the uncontrollable hydrolysis of tin(IV) and nearly identical trends of the 3d metals (b) Ligand electronegativity (χ_{ligand}) as a function of pH for the Sn−F complexation relationship, showing a wide pH stability window for the complexation of $[Sn(H_2O)_5F]^{3+}$ bordered by ionic (F^-) and hydrolytic (HF) dissociation. (c) Logarithm of the formation constant, Q_{xy}, for the mononuclear (Q_{11}), dinuclear (Q_{21}), and partial charge model predicted mononuclear (Z_{11}) products.

capillaries were recorded at beamline 11-BM at the Advanced Photon Source at Argonne National Laboratory using a photon wavelength of 0.4124(1) Å.[12] Discrete detectors covering finite angular ranges were scanned over a 34° 2θ range, with data points collected every 0.001° 2θ. A mixture of NIST standard reference materials, Si (SRM 640c) and Al_2O_3 (SRM 676), was used to calibrate the instrument, where the Si lattice constant determines the wavelength for each detector, before merging the data into a single set of intensities evenly spaced in 2θ.

LeBail profiling matching was employed by the General Structure Analysis System (GSAS)[13,14] to obtain the lattice parameters, profile terms, and $|F_{obs}|$ within the $Pn\bar{3}$ space group. Using atom positions initialized from ref 7, we confirmed the atom positions by Rietveld refinement[15] in GSAS. The full-width-at-half-maximum (fwhm) for selected Bragg reflections were calculated by hand. Maximum entropy method (MEM) pattern fitting[16] was performed with Rietan-2000[17] and PRIMA[18] to determine the distribution of electron density within the unit cell. Bond valence sums were calculated using VALIST.[19] The structures and electron density were visualized using the software VESTA.[20]

Magnetic Characterization. Magnetic measurements were performed using a SQUID magnetometer (MPMS XL5, Quantum Design, Inc.). Powders were sealed into a gelatin capsule and embedded in paraffin wax molten around the particles at 55 °C. The magnetic susceptibilities were

dx.doi.org/10.1021/ic1025075 |*Inorg. Chem.* 2011, 50, 3003–3009

measured from 2 to 300 K with cooling in zero field and in field (0.01 T for the manganese compound, 5 T for cobalt). The induced magnetization was determined by sweeping the field ±5 T at 2 K. No magnetization loops were seen; instead, Brillouin functions were observed.

RESULTS AND DISCUSSION

Kinetically Controlled Hydrolysis. Of the precursors utilized in this study, only solutions containing the hydrated salts of Mn(II) and Co(II) produced material from the kinetically controlled, low-temperature catalytic hydrolysis and subsequent polycondensation. We contribute an understanding of their distinct reactivities with a discussion of their spontaneous hydrolysis behaviors. A key requirement for the formation of the ordered double perovskite hydroxide is the prevention of uncontrolled spontaneous hydrolysis of the metal salts in solution.

Tin(IV) is prone to fast and uncontrolled hydrolysis in solution, as noted by the fuming precipitation of tin oxide when $SnCl_4$ is exposed to humid atmospheres. This is suitably predicted from a partial charge model of electronegativities, as described by Livage et al.[21,22] We calculate that an unprotected $Sn^{4+}_{(aq)}$ specie has a hydrolysis ratio greater than 2 at a pH as low as 0 (Figure 2). For the reaction

$$Sn^{4+} + yH_2O \rightleftharpoons Sn(OH)_y^{(4x-y)+} + yH^+ \qquad (1)$$

Nazarenko, et al.[23] determined reaction quotients, Q_y = 0.57, 0.63, 0.36, and −0.86 for y = 1, 2, 3, and 4, respectively. When the partially hydrolyzed complex is a majority product, spontaneous condensation drives precipitation of the hydroxide or oxohydroxide.[21,24] Therefore, it is important to stabilize small precursor cations of high positive charge against uncontrolled partial hydrolysis.

Fluorine−tin(IV) complexes are exceptionally stable and acidic, as predicted by the empirical relationship relating the cation charge to its size:[25]

$$\log Q = -1.56 + \frac{0.48Z_+^2}{r_+} \qquad (2)$$

Using Z_{Sn} = 4 and r_{Sn} = 0.69, the reaction quotient for $Sn^{4+} + F^- = [SnF]^{3+}$ is log Q = 9.57. Thus, one can isolate stable hexafluorostannate complexes that undergo controlled partial hydrolysis in aqueous solutions.

Calculations from the partial charge model predict that a $[Sn(H_2O)_5F]^{3+}$ is stable against ionic and hydrolytic dissociation of the anion over a large pH range from −6 to 8 [Figure 2b]. The degree of hydrolysis (h) decreases with increasing concentration, such that at 0.111 M concentrations of $[SnF_6]^{2-}$, h = 0.02; for 0.066 M, h = 0.031, and at 0.04 M, h = 0.044.[26] At a working concentration of 0.1 M $[SnF_6]^{2-}$, as in the reactions studied here, the degree of hydrolysis at low pH is reduced.

In hexafluoroantimonate solutions, stepwise hydrolysis occurs with easy removal of the first fluorine ligand, followed by slow release of the remaining ligands.[27] Similar characteristics have been attributed to tin from the stability of $[SnF_5X]^{2-}$ species, where X = OH^-, Cl^-, and Br^-,[28] further supporting our conclusion that tin−fluorine anions are hydrolyzed in basic conditions.[25]

The partial charge model does not predictively distinguish the hydrolysis behaviors of any of the divalent transition metal ions [Figure 2a]. In fact, Co(II) and Cu(II) have the same electronegativity and are superimposable. Therefore, we utilize data tabulated from ref 24 regarding the equilibrium behavior of the transition metals (Table 2).

Table 2. Formation Quotients, Q_{xy}, for Divalent First Row Transition Metal Ions at 25°C for $xM^{2+} + yH_2O \rightleftharpoons M_x(OH)_y^{(2x-y)+} + yH^+$, Tabulated from Ref 24

$\log(Q_{xy})$	Mn^{2+}	Fe^{2+}	Co^{2+}	Ni^{2+}	Cu^{2+}	Zn^{2+}
$\log(Q_{11})$	−10.46	−9.5	−10.2	−10.5	−8.0	−9.12
$\log(Q_{21})$	−9.87		−9.37	−6.5	−10.95 (Q_{22})	−7.48
$\log(Q_{23})$	−25.47					
$\log(Q_{44})$			−29.30	−27.37		

Spontaneous hydrolysis is described by the reaction

$$xM^{2+} + yH_2O \rightleftharpoons M_x(OH)_y^{(2x-y)+} + yH^+ \qquad (3)$$

with the formation product, Q_{xy}. For Mn(II), Co(II), Ni(II), and Zn(II), dinuclear products (Q_{21}) are favored (Table 2). For Cu(II), only mononuclear complexes are reported. From partial charge model calculations [Figure 2a], we estimate a mononuclear formation constant (Z_{11}) by subtracting the pH at which the hydrolysis ratio is 1 from the equilibrium constant for the dissociation of water, 14. The tabulated and predicted results are shown graphically in Figure 2c. While the partial charge model is oversimplified, it does a reasonable job of approximating the hydrolysis behavior of several of the divalent cations.

In the context of kinetically controlled hydrolysis, it is essential to understand the starting reactants before the hydrolytic catalyst, $NH_{3(g)}$, is introduced. The formation constants for Mn(II) and Co(II) are reasonably clustered, indicating predictively controllable hydrolysis behavior. However, Ni(II), Cu(II), and Zn(II) do not share these attributes, which may explain the inability to form double perovskite hydroxides with tin under kinetic control.

Hydrolysis of nickel(II) strongly favors the formation of dinuclear hydrolysis products. From its aqueous reaction with tin and ammonia, the only notable precipitate we obtained was a green powder, consistent with a poorly structured $Ni(OH)_2$ as revealed by X-ray diffraction (data not shown). Therefore, we conclude that the increased disposition for nickel to self-associate during hydrolysis prevents it from forming stoichiometrically ordered compounds with other metals.

In reactions containing copper, the thin film grown at the meniscus quickly collapsed, preventing the isolation of product formed solely by kinetically controlled hydrolysis and subsequent polycondensation. Formation of the monometallic spontaneous hydrolysis product of Cu(II)-containing precursors is more favorable than for the other transition metals, indicating that it may have spontaneously hydrolyzed to a degree incompatible with the attack of $[SnF_5(OH)]^{2-}$ complexes. Further hydrolysis neutralizes the partial positive charge of $Cu^{2+}_{(aq)}$, thereby reducing the electrostatic attraction between the tin and copper complexes. Additionally, the Jahn−Teller distortions of Cu(II) may reduce any favorable lattice energy that could otherwise drive formation of the product. Consistent with this suggestion, Kramer et al. reported a tetragonal lattice for the $CuSn(OH)_6$ structure when produced from metathesis of $Na_2SnO_3 \cdot nH_2O$ and $CuCl_2 \cdot 6H_2O$.[11]

Reactions with zinc were unsuccessful because of the amphoteric nature of $Zn^{2+}_{(aq)}$ which results in the formation of ZnO under kinetic control.[29] The formation of ordered $BSn(OH)_6$ compounds is favored by the kinetically limited and stepwise hydrolysis of $[SnF_6]^{2-}$, and its ability to interact with well-behaved partially hydrolyzed transition metal complexes. Of the divalent metals studied, only cobalt and manganese share these characteristics.

Structure. The manganese compound, $MnSn(OH)_6$, is a colorless powder; whereas the cobalt compound, $CoSn(OH)_6$, is pink [Figure 3b,d]. The pink color of octahedrally coordinated

dx.doi.org/10.1021/ic1025075 |Inorg. Chem. 2011, 50, 3003–3009

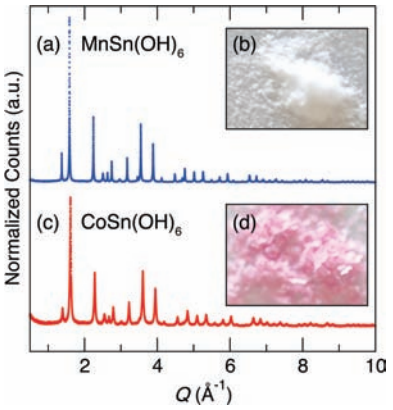

Figure 3. (a,c) High-resolution synchrotron X-ray powder diffraction from beamline 11-BM at the Advanced Photon Source of (a) $MnSn(OH)_6$ (blue) and (b) $CoSn(OH)_6$ (red) showing reflections out to 10 Å. (b,d) Photographs of (c) $MnSn(OH)_6$ and (d) $CoSn(OH)_6$ illustrate the colorless manganese and bright pink cobalt in these materials.

Table 3. Estimated Crystalline Correlation Lengths (D_p) for Different Lattice Planes (hkl) Calculated Using the Scherrer Equation from the Bragg Reflection Peak Widths[a]

(hkl)	(111)	(200)	(220)	**(310)**	(222)	**(312)**	(400)
$MnSn(OH)_6$	67.3	60.3	53.5	**21.9**	48.0	**14.5**	48.1
$CoSn(OH)_6$	17.2	18.6	16.8	**12.9**	16.0	**10.6**	15.9

[a] Units are in nm.

cobalt is indicative of a strong octahedral distortion to break the Laporté forbidding inversion symmetry.[30] Further elucidation of the structure and bonding is provided from high-resolution synchrotron X-ray diffraction.

The crystalline powders of both $MnSn(OH)_6$ and $CoSn(OH)_6$ show Bragg reflections to $Q = 10$ Å^{-1} (Figure 3), despite the low temperature, kinetically controlled preparation. The tabulated crystalline correlation lengths (D_p, Table 3) were calculated using the Scherrer equation, $D_p = (K\lambda)/(\beta \cos \theta)$, where the shape factor, $K = 0.94$, $\lambda = 0.4124$ Å, β is the full-width at half-maximum in radians, and θ is half of the diffracted angle for the corresponding Bragg plane. The $MnSn(OH)_6$ compound has larger correlation lengths by this metric, although both compounds show anisotropic broadening of reflections corresponding to (310) and (312) Bragg planes, which may reflect an extent of anti-site disorder.

Pattern fitting performed by the maximum entropy method (MEM) initialized with the structure from ref 7 allows image restoration of the electron density within a unit-cell (Figure 4). The isosurface at 3 e Å^{-3} in Figure 4a confirms the expected lattice of tilted metal−oxygen octahedra, depicted in Figure 1. The differences in localized electron density, emphasized from a section along the (310) plane in Figure 4b, are significantly distinguishing between the tin, transition metal, and oxygen sites. Furthermore, the logarithmic contour lines illustrate the absence of overlapping electron density, thus indicating a strong ionic bonding character of the μ-(OH) ligands.

Rietveld refinement, shown in Figure 5 and in Figure 6, confirms the atom positions from the localization of electron density in the MEM analysis. The atom positions (Table 4) reveal tilting of distorted octahedra, with $CoSn(OH)_6$ showing greater deviations from 90° octahedral bond angles (O_h distortion) and 180° M−O−Sn bond angles (Table 5). The partial

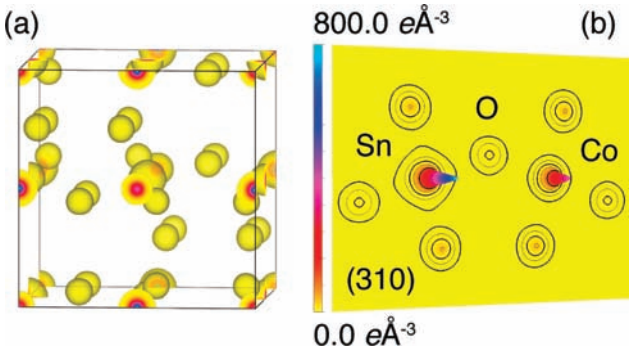

Figure 4. (a) Electron density from maximum entropy minimization (MEM) for $CoSn(OH)_6$ showing the overall distribution of electron density in the unit cell at an isosurface level of 3 e Å^{-3}. (b) The distinguishing electron density between tin (left) and the transition metal (right), shown with a z-axis scaling of the (310) planes. Logarithmic contour lines (thick lines for an order of magnitude; thin lines are midpoints ranging from 1 to 500 e Å^{-3}) indicate a lack of overlapping electron densities between the μ-(OH) and the metal sites, suggestive of ionic, rather than covalent bonding. The colored electron density scale describes both (a) and (b).

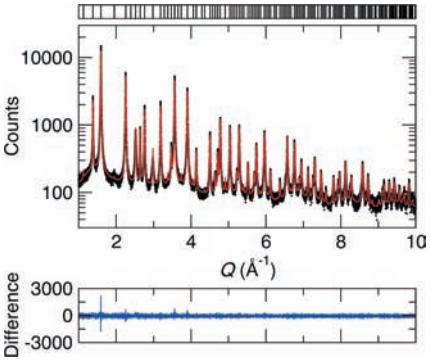

Figure 5. Rietveld refinement of diffraction data for $MnSn(OH)_6$ showing, on a logarithmic scale, the observed (black dots), calculated (red line), and difference (blue line, below) profiles. The hashes above each curve indicate the expected Bragg reflections for the $Pn\bar{3}$ space group.

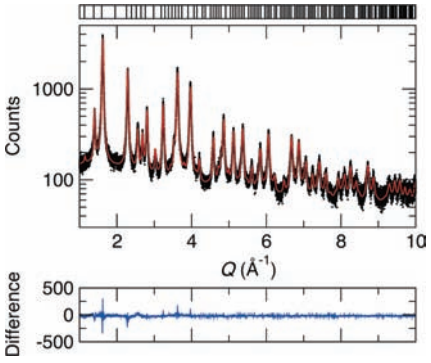

Figure 6. Rietveld refinement of diffraction data for $CoSn(OH)_6$ showing, on a logarithmic scale, the observed (black dots), calculated (red line), and difference (blue line, below) profiles. The hashes above each curve indicate the expected Bragg reflections for the $Pn\bar{3}$ space group.

occupancy of tin on the transition metal site [Sn(2)] confirms a modicum of anti-site disorder.

dx.doi.org/10.1021/ic1025075 |Inorg. Chem. 2011, 50, 3003–3009

Table 4. Crystallographic Summary within the $Pn\bar{3}$ Space Group for Both $MnSn(OH)_6$ [a = 7.884563(21) Å, V_{cell} = 490.1544(23) Å^3] and $CoSn(OH)_6$ [a = 7.75973(5) Å, V_{cell} = 467.240(5) Å^3] Showing the Atom Positions, Atomic Displacement Parameters, and Site Occupancies[a]

Compound/Site	x	y	z	$U_{iso} \times 100$	g
			$MnSn(OH)_6$		
Mn(1)	0.5	0.5	0.5	1.558(31)	0.843(2)
Sn(1)	0	0	0	1.071(9)	1
Sn(2)	0.5	0.5	0.5	1.071(9)	0.157(2)
O(1)	0.5619(4)	0.42445(33)	0.7592(5)	0.98(4)	1
H(1)	0.052(4)	0.0608(28)	0.249(5)	0.5	1
			$CoSn(OH)_6$		
Co(1)	0.5	0.5	0.5	0.571(27)	0.895(3)
Sn(1)	0	0	0	0.801(12)	1
Sn(2)	0.5	0.5	0.5	0.801(12)	0.105(3)
O(1)	0.5585(4)	0.42001(31)	0.7557(4)	−0.43[b]	1
H(1)	0.044(4)	0.0457(29)	0.260(5)	0.5	1

[a] Refinement statistics. $MnSn(OH)_6$: χ^2=2.21, R_{wp} = 9.6%, R_{F^2} = 4.8% ; $CoSn(OH)_6$: χ^2=1.19, R_{wp} = 7.7%, R_{F^2} = 4.5%. [b] Anisotropic atomic displacement parameters (×100): U_{11} = 0.73(16), U_{22}=−0.22(13), U_{33}=−1.81(8), U_{12}=−0.18, U_{13} = 0.96(16), U_{23}=−1.28(16).

Table 5. Crystallographic and Bond Valence Sum Results

	M−O−Sn	O_h distortion		Sn BVS	
B	angle	Sn/M	M BVS	Sn(1)/Sn(2)	O BVS
Mn	137.3°	6.8°/6.1°	2.1	4.1/2.8	1.0
Co	136.7°	8.2°/7.9°	1.9	4.1/3.3	1.0

Even though protons carry no electron density with which to scatter electrons, the hydrogen positions improved the fit to the data in Rietveld refinements for both compounds, and settled to a stable position. This is typically only accomplished in single-crystal X-ray studies with sufficient data quality.[31] A broad minimum in the normalized goodness-of-fit (χ^2/χ_0^2) as a function of distance from the ideal position (Figure 7) indicates static disorder of the proton of ±0.2 Å from the reasonable bond distance of 1 Å from oxygen. A previous neutron diffraction study of $MnSn(OH)_6$ located the hydrogen nucleus at an orientation 180° with respect to the ⟨100⟩ crystal directions from the position reported here.[6] We acknowledge that our results may be evidence of a small degree of anti-site or tilting disorder, rather than an indication of the proton positions in the structures.

Bond valence sums (BVS) indicate an empirical preference for oxidation states based on crystallographic bond distances.[32] The BVS tabulated for both compounds (Table 5) confirm the oxidation states of 2+ for both transition metals and tin(IV). Additionally, the oxygen BVS indicates an effective oxidation state of 1+, confirming that the oxygen is a bridging hydroxo ligand [μ-(OH)], rather than an oxo ligand.

Magnetism. The magnetic properties of $MnSn(OH)_6$ and $CoSn(OH)_6$ were measured from 2 K to 300 K. Both compounds behave as paramagnets, clearly demonstrating the absence of impurity $Mn(OH)_2$ or $Co(OH)_2$ phases, which antiferromagnetically order near 10 K.[33,34]

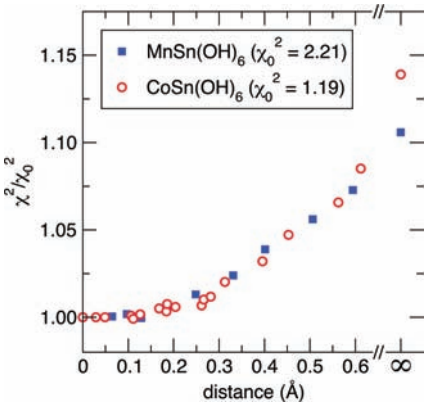

Figure 7. Normalized goodness-of-fits (χ^2) as a function of distance of hydrogen from the ideal positions (χ_0^2) from Rietveld refinements of synchrotron X-ray powder diffraction data for $MnSn(OH)_6$ (filled blue squares) and $CoSn(OH)_6$ (open red circles); exclusion of hydrogen is indicated at infinite separation (∞).

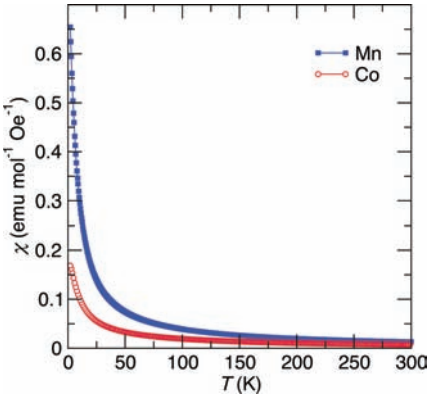

Figure 8. Temperature dependence of the magnetic susceptibility demonstrating identical behavior in zero-field and field cooling (0.01 T for Mn, 5 T for Co) for $MnSn(OH)_6$ (blue closed squares) and $CoSn(OH)_6$ (red open circles).

The temperature dependent magnetic susceptibility, $\chi(T)$, shows no history dependence of an applied field, indicating the absence of a phase transition to long-range magnetic order or freezing of a spin glass (Figure 8). The susceptibility follows a Curie−Weiss law (CW) dependence on temperature after the subtraction of a temperature independent (diamagnetic) component:

$$\chi = \frac{C}{T - \Theta_{CW}} + \chi_0 \qquad (4)$$

Linear fits from 200 K to 300 K to the inverse susceptibility from eq 4 provide the Curie constant (C), the Weiss temperature (Θ_{CW}), and diamagnetic susceptibility (χ_0), as summarized in Table 6. After subtracting the diamagnetic contribution, the data are nondimensionally linearized as

$$\frac{C}{(\chi - \chi_0)|\Theta_{CW}|} + \mathrm{sgn}(\Theta_{CW}) = \frac{T}{|\Theta_{CW}|} \qquad (5)$$

This normalization, plotted in Figure 9, indicates that $MnSn(OH)_6$ exhibits nearly ideal paramagnetic behavior down to 2 K. However, $CoSn(OH)_6$ deviates from ideal paramagnetism with

dx.doi.org/10.1021/ic1025075 |Inorg. Chem. 2011, 50, 3003–3009

Table 6. Curie-Weiss Parameters of $BSn(OH)_6$ Extracted from a Linear Fit to $1/(\chi - \chi_0) = (T - \Theta_{CW})/C$ at High Temperatures (200 K to 300 K) and Expected High-Spin Effective Moment for Different Spin-Orbital Contributions

	experimental			expected μ_{eff}		
	Θ_{CW}	μ_{eff}	χ_0	J coupling;	$L+S$	spin only
M	[K]	[μ_B mol^{-1}]	[μ_B mol^{-1}]	[μ_B mol^{-1}]		
Mn	−3.8	5.78	-1.25×10^{-7}	5.92	5.92	5.92
Co	−27.9	4.51	-1.37×10^{-7}	6.63	5.20	3.87

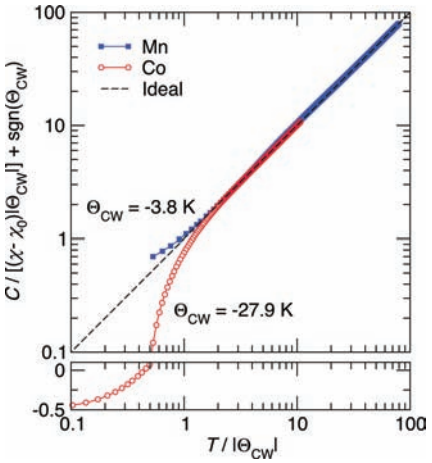

Figure 9. Temperature normalized inverse susceptibility under field cooling (0.01 T for Mn, 5 T for Co) from a Curie−Weiss analysis for $MnSn(OH)_6$ (blue closed squares) and $CoSn(OH)_6$ (red open circles) indicating ideal behavior of the Mn compound, but uncompensated deviations from Curie−Weiss behavior of the $CoSn(OH)_6$ near 27.9 K, despite an antiferromagnetic mean-field interaction ($\Theta_{CW} < 0$).

uncompensated spin interactions near 28 K, yet exhibits an antiferromagnetic mean-field interaction ($\Theta_{CW} < 0$).

From this analysis, we calculate an effective moment per magnetic cation, μ_{eff}. The effective moment per Mn^{2+} approaches the expected spin-only value for $S = 5/2$. For Co^{2+}, μ_{eff} shows a combination of both spin and orbit contributions to the total moment (Table 6). To observe how the effective moment changes as a function of temperature, we plot in Figure 10 the effective moment:

$$\mu_{eff} = \frac{1}{\mu_B}\sqrt{\frac{3k_B[\chi(T) - \chi_0](T - \Theta_{CW})}{N_A}} \qquad (6)$$

with the experimentally measured $\chi(T)$, Θ_{CW}, and χ_0 from the CW analysis as inputs to the formula, where μ_B is the Bohr magneton, k_B the Boltzmann constant, and N_A is Avogadro's number.

One expects spin−orbit coupling to decrease μ_{eff} of $CoSn(OH)_6$ at low temperatures.[35] For $MnSn(OH)_6$, which has no orbital momentum, this effect is negated. The effective moment of $MnSn(OH)_6$ decreases below 8 K, attributed to either weak antiferromagnetic interactions or zero-field splitting of the $S = 5/2$ ground state. However, $CoSn(OH)_6$ exhibits a sharp rise in μ_{eff} at low temperatures (Figure 10). We attribute this behavior both to the strong single-ion anisotropy of cobalt(II)[36] which prevents the free rotation of spins at low temperature and

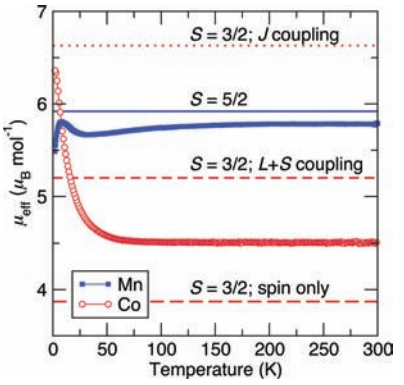

Figure 10. Effective moment (μ_{eff}) as a function of temperature for $MnSn(OH)_6$ (blue closed squares) and $CoSn(OH)_6$ (red open circles) along with the corresponding expected spin only, $L+S$, and J coupling effective moments.

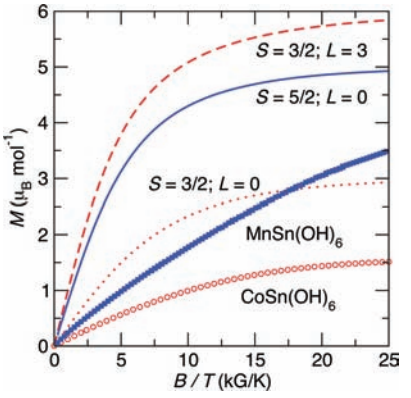

Figure 11. Induced magnetization at 2 K for $MnSn(OH)_6$ (blue closed squares) and $CoSn(OH)_6$ (red open circles) and the corresponding Brillouin functions for $S = 3/2$; $L = 0$ (dotted red line), $S = 3/2$; $L = 3$ (dashed red line), and $S = 5/2$; $L = 0$ (blue solid line).

to a larger number of surface spins. Both characteristics act to increase the effective moment at low temperatures and yield an uncompensated moment. This is further supported by the negative deflections from ideality seen in Figure 9 for $CoSn(OH)_6$.

The field dependence of the magnetization at low temperatures also supports the paramagnetic nature of the compounds, as seen from the observation of Brillouin functions (Figure 11). The induced magnetization at 2 K also reveals spin interactions consistent with $\Theta_{CW} < 0$. The magnetizations of both compounds studied here are depressed from the expected values, even considering a fully quenched orbital contribution for Co^{2+} ($S = 3/2$; $L = 0$). Therefore, the negative values of Θ_{CW} accurately reflect antiferromagnetic interactions, which expectedly decrease the observed magnetization. The data from both compounds do not match the exact curvature of the ideal Brillouin functions; for $MnSn(OH)_6$, this reflects weak antiferromagnetic interactions rather than observation of zero-field splitting of the single-ion ground state. $CoSn(OH)_6$ has a lower expected moment than does $MnSn(OH)_6$, consistent with having a larger mean field interaction strength, $|\Theta_{CW}|$.

From the strongly ionic character of M−O−Sn bonding (Figure 4) and exceptionally long through-space distances between magnetic cations, we would not anticipate a transition to magnetic order. However, the nonzero orbital momentum of

dx.doi.org/10.1021/ic1025075 |Inorg. Chem. 2011, 50, 3003–3009

the cobalt spins induces a single-ion anisotropy, creating the increased effective moment and deviations from ideal Curie−Weiss behavior. The magnetic properties reflect a sufficient degree of ordering of the B and B' sites in the material, as clusters of simple transition metal hydroxides would yield significantly different magnetic properties.

CONCLUSION

From kinetically controlled aqueous hydrolysis of selected precursors, we demonstrate that careful ligand and cation selection can yield complex, ordered compounds starting from simple salt solutions without the input of additionally energy. The isolated compounds, $MnSn(OH)_6$ and $CoSn(OH)_6$, crystallize in an ordered double perovskite lattice, $BB'(OH)_6$, with an empty A site exhibiting the connectivity of ReO_3. The metal−oxygen octahedra are tilted, with some anti-site disorder. Maximum entropy electron density distributions indicates an ionic bonding character between the metals and the oxygen. While both compounds are paramagnetic down to 2 K, $CoSn(OH)_6$ exhibits spin interactions at low temperatures. The weak and cooperative interactions during hydrolysis and polycondensation are complex and transient; therefore, it is essential to first understand the starting and final conditions of the synthesis reactions, as studied here.

AUTHOR INFORMATION

Corresponding Author

*E-mail: d_morse@lifesci.ucsb.edu. Fax:+001-805-893-7998. Phone:+001-805-893-7442.

ACKNOWLEDGMENT

The authors thank B. Schwenzer and B. C. Melot for helpful discussions and the expert beamline 11-BM staff (L. Rybud, M. Suchomel, and B. Toby) for the use of their outstanding diffractometer. J.R.N. gratefully thanks the National Science Foundation for support through the Graduate Research Fellowship. J.A.K. thanks the ConvEne-IGERT Program (NSF-DGE 0801627) for an Associateship. This research was additionally supported by grants from the U.S. Department of Energy, Office of Basic Energy Science to DEM (DEFG03-02ER46006) and to J.A.K. (DE-FG02-10ER16081); and by use of the Advanced Photon Source supported by the U.S. Department of Energy, Office of Science, Office of Basic Energy Sciences, under Contract No. DE-AC02-06CH11357, and UCSB's Materials Research Laboratory (MRL) Central Facilities, supported by the MRSEC Program (NSF, Award No. DMR05-20415). The MRL is a member of the NSF-funded Materials Research Facilities Network (www.mrfn.org).

REFERENCES

(1) Neilson, J. R.; Schwenzer, B.; Seshadri, R.; Morse, D. E. *Inorg. Chem.* **2009**, *48*, 11017–11023.
(2) Niesz, K.; Reji, C.; Vargas, R.; Neilson, J. R.; Morse, D. E. *Cryst. Growth Des.* **2010**, *10*, 4485–4490.
(3) Brutchey, R. L.; Morse, D. E. *Angew. Chem., Int. Ed.* **2006**, *45*, 6564–6566.
(4) Nefedov, E. I.; Griffin, W. L.; Kristiansen, R. *Can. Mineral.* **1977**, *15*, 437–445.
(5) Moore, P. B.; Smith, J. V. *Arkiv Mineral. Geol.* **1966**, *4*, 395–399.
(6) Basciano, L. C.; Peterson, R. C.; Roeder, P. L.; Swainson, I. *Can. Mineral.* **1998**, *36*, 1203–1210.
(7) Christensen, A. N.; Hazell, R. G. *Acta Chem. Scand.* **1969**, *23*, 1219–1224.
(8) Jena, H.; Kutty, K. V. G.; Kutty, T. R. N. *Mater. Chem. Phys.* **2004**, *88*, 167–179.
(9) Fu, X.; Wang, X.; Ding, Z.; Leung, D. Y. C.; Zhang, Z.; Long, J.; Zhang, W.; Li, Z.; Fu, X. *Appl. Catal. B* **2009**, *91*, 67–72.
(10) Inagaki, M.; Kuroishi, T.; Yamashita, Y.; Urata, M. *Z. Anorg. Allg. Chem.* **1985**, *527*, 193–202.
(11) Kramer, J. W.; Kelly, B.; Manivannan, V. *Cent. Eur. J. Chem.* **2010**, *8*, 65–69.
(12) Wang, J.; Toby, B. H.; Lee, P. L.; Ribaud, L.; Antao, S. M.; Kurtz, C.; Ramanathan, M.; Dreele, R. B. V.; Beno, M. A. *Rev. Sci. Instrum.* **2008**, *79*, 085105.
(13) Larson, A. C.; Dreele, R. B. V. Los Alamos National Laboratory Report LAUR 2000, pp 86−748
(14) Toby, B. H. *J. Appl. Crystallogr.* **2001**, *34*, 210–213.
(15) Rietveld, H. M. *J. Appl. Crystallogr.* **1969**, *2*, 65–71.
(16) Izumi, F. *Solid State Ionics* **2004**, *172*, 1–6.
(17) Izumi, F.; Ikeda, T. *Mater. Sci. Forum* **2000**, *321−324*, 198–203.
(18) Izumi, F.; Dilanian, R. A. In *Recent Research Developments in Physics*; Transworld Research Network: Trivandrum, Kerala, India, 2002; Vol. 3, Part II, pp 699−726.
(19) Wills, A. S.; Brown, I. D. *VALIST*; http://www.ucl.ac.uk/chemistry/staff/academic_pages/andrew_wills.
(20) Momma, K.; Izumi, F. *J. Appl. Crystallogr.* **2008**, *41*, 653–658.
(21) Livage, J.; Henry, M.; Sanchez, C. *Prog. Solid State Chem.* **1988**, *18*, 259–341.
(22) Henry, M.; Jolivet, J.-P.; Livage, J. . In *Chemistry, Spectroscopy and Applications of Sol-Gel Glasses*; Springer: Berlin, 1992; Vol. 77, pp 153−206.
(23) Nazarenko, V. A.; Anotonovich, V. P.; Nevskaya, E. M. *Russ. J. Inorg. Chem.* **1971**, *16*, 980.
(24) Baes, C. F.; Mesmer, R. E. *The Hydrolysis of Cations*; Wiley: New York, , 1976.
(25) Cotton, F. A.; Wilkinson, G. *Advanced Inorganic Chemistry*; Wiley: New York, 1988.
(26) Schmitt, R. H.; Grove, E. L.; Brown, R. D. *J. Am. Chem. Soc.* **1960**, *82*, 5292–5295.
(27) Mazeika, W. A.; Neumann, H. M. *Inorg. Chem.* **1966**, *5*, 309–311.
(28) Dillon, K. B.; Marshall, A. *J. Chem. Soc., Dalton Trans.* **1984**, 1245.
(29) Kisailus, D.; Schwenzer, B.; Gomm, J.; Weaver, J. C.; Morse, D. E. *J. Am. Chem. Soc.* **2006**, *128*, 10279–10280.
(30) Lever, A. B. P. *Inorganic Electronic Spectroscopy*; Elsevier: New York, 1968.
(31) Hawthorne, F.; Sokolova, E. *Can. Mineral.* **2002**, *40*, 939–946.
(32) Urusov, V. S.; Orlov, I. P. *Kristallografiya* **1999**, *44*, 736–760.
(33) Christensen, A. N.; Ollivier, G. *Solid State Commun.* **1972**, *10*, 609–614.
(34) Takada, T.; Bando, Y.; Kiyama, M.; Miyamoto, H. *J. Phys. Soc. Jpn.* **1966**, *21*, 2726.
(35) Kotani, M. *J. Phys. Soc. Jpn.* **1949**, *4*, 293–297.
(36) Kanamori, J. *Prog. Theor. Phys.* **1957**, *17*, 197–222.